S1 Estimation of the inconsistency in the elastic effect

There is an inconsistency in the applied methodology when taking into account elastic deformations that occur due to contemporary changes in ice mass (i.e. changes in uplift). One of the results of the data combination is a smoothed IMC. However, the spatial resolution of the smoothed IMC is insufficient to account for the true elastic effects observed with GNSS on bedrock. The true elastic effects would be underestimated, e.g. in the vicinity of high-magnitude IMC at small spatial scales. For this reason, we determine a high-spatial resolution elastic effect from the surface elevation changes and the FAC changes directly (Sect. 3). To do so, we use the GIA result from the data combination to correct the altimetry data for GIA. However, this GIA estimate is already based on the mentioned data sets, which is inconsistent. Figure S1 illustrates the elastic effect that we calculate from the (smooth) IMC from the data combination. The figure additionally shows the high-resolution elastic effect and a Gaussian smoothed variant of the high-resolution variant using the Gaussian filter of the optimal result (135 km half-response width). The difference between the elastic effect based on the smooth IMC of the data combination and the smoothed high-resolution elastic effect highlights this inconsistency. It is less than 0.5 mm/a in magnitude at maximum and less elsewhere. From this, we conclude that for investigations in this region it is only a relative minor effect that we can ignore. In regions where signals with small magnitudes are present, iterations of the data combination as shown by Sasgen et al. (2017) could minimize this inconsistency.

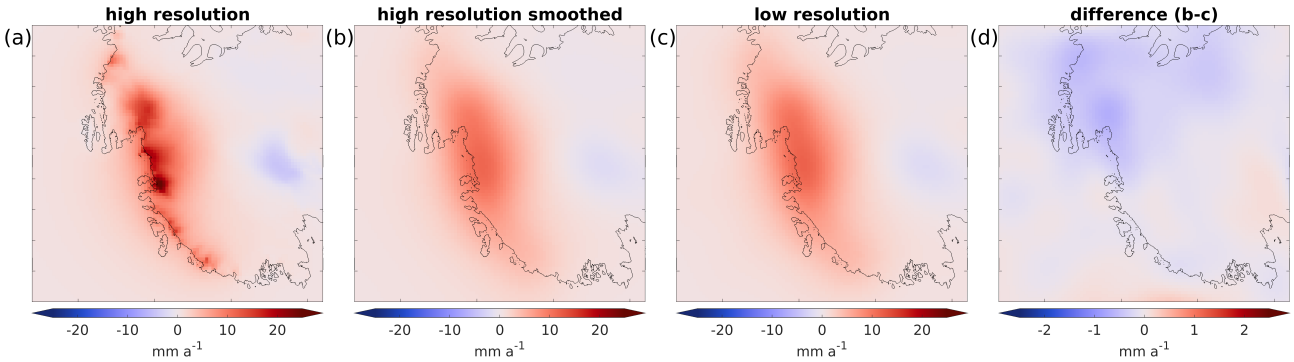

Figure S1: Comparison of the elastic-related bedrock motion: (a) a high resolution elastic bedrock motion based on altimetry data that was corrected for GIA resulting from the data combination. (b) the same as in (a) but the Gaussian smoother of the optimal result is applied (135 km half-response width). (c) A low resolution elastic effect that is estimated directly from the IMC resulting from the data combination. (d) The difference (b−c) of these two variants. Note the different value range in (d) to highlight the differences.

S2 Supplemental figures

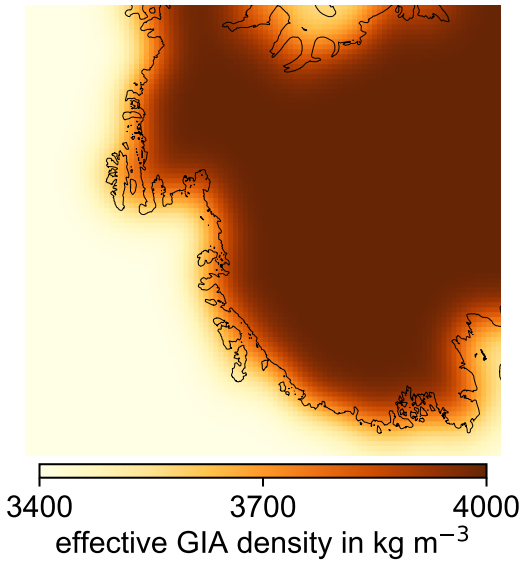

Figure S2: Map of the effective GIA density (Eq. 7), i.e. the ratio of GIA-induced surface density changes and GIA-induced bedrock motion generated according to Riva et al. (2009).

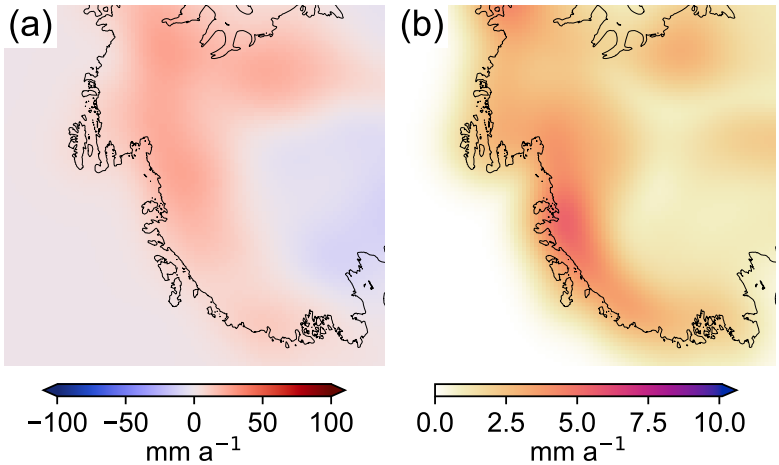

Figure S3: (a) Map of the smoothed rate of firn air content (FAC), i.e. a smoothed variant of Fig. 1c and (b) map of the 2-σ-FAC-uncertainty, FAC covariances are obtained from Willen et al. (2022).

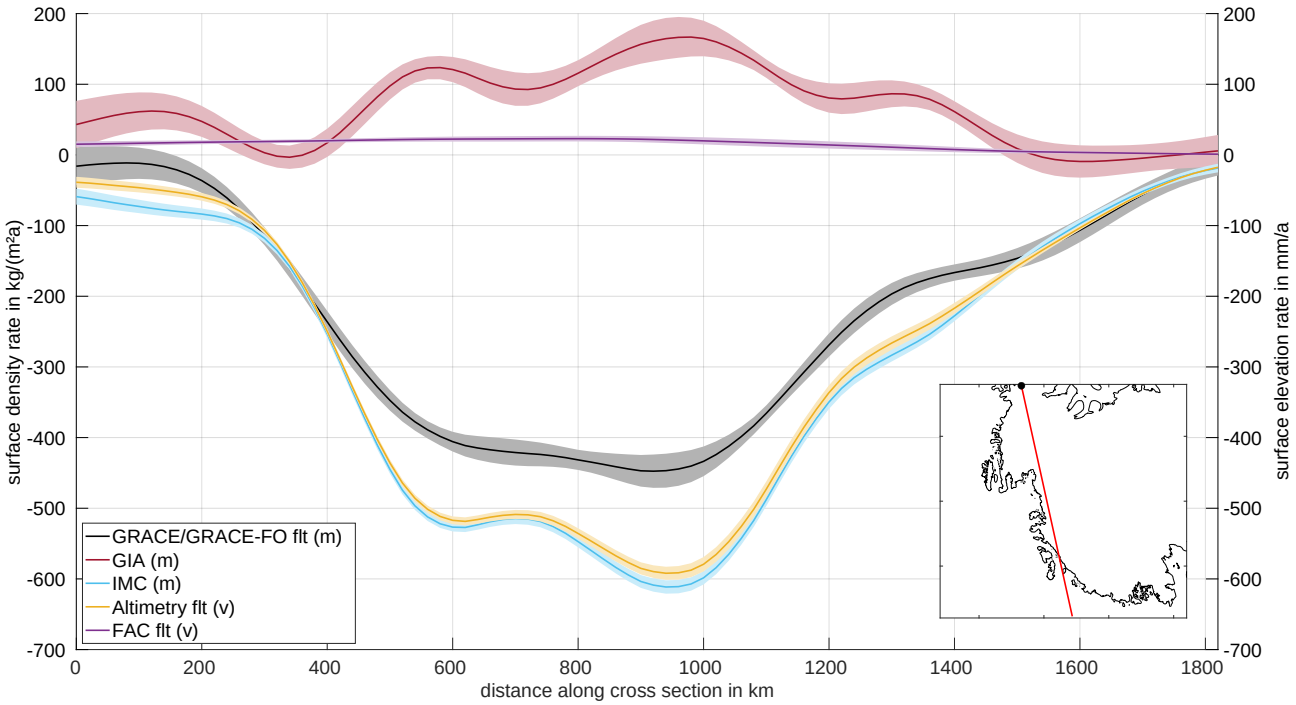

Figure S4: Mean rates with 2-σ-uncertainties from smoothed input data and the optimal data combination result (135 km half-width Gaussian smoothing) along a transect through the Amundsen Sea Embayment, indicated with the red line in the lower right corner inset. The transect start distance of 0 km (horizontal axis) corresponds to the black dot in the inset. Surface density changes and surface elevation changes, i.e. mass changes and volume changes, are indicated with (m) and (v), respectively, within the legend and refer to the left and right vertical axis, respectively.

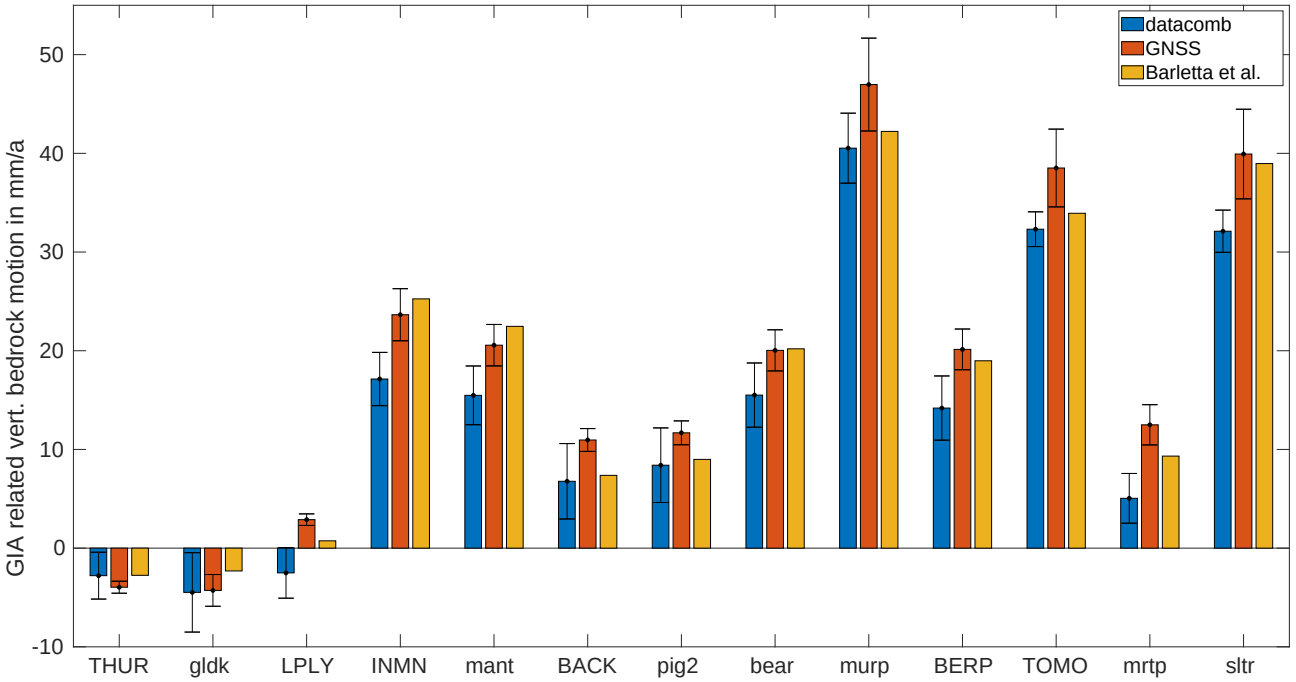

Figure S5: Comparison of bedrock motion at GNSS sites similar as illustrated in Figure 2c but showing the GIA-related part only. Additionally we include the modelled GIA-related bedrock motion from Barletta et al. (2018) that best fits GNSS data. For GNSS-sites with more than three years of continuous data the names are given in upper case.

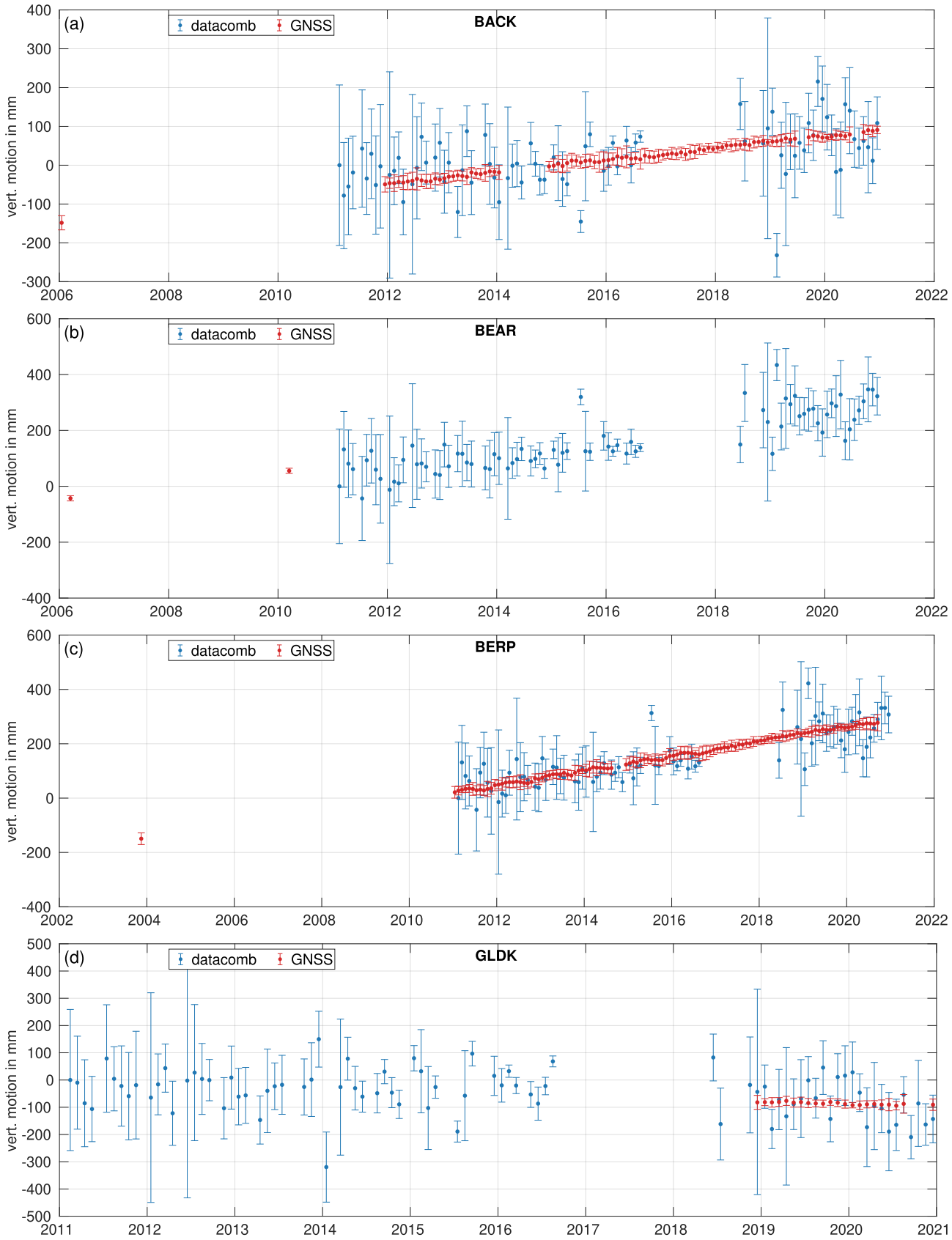
(a)
datacomb
GNSS
BACK
vert. motion in mm
(b)
BEAR
(c)
BERP
(d)
GLDK

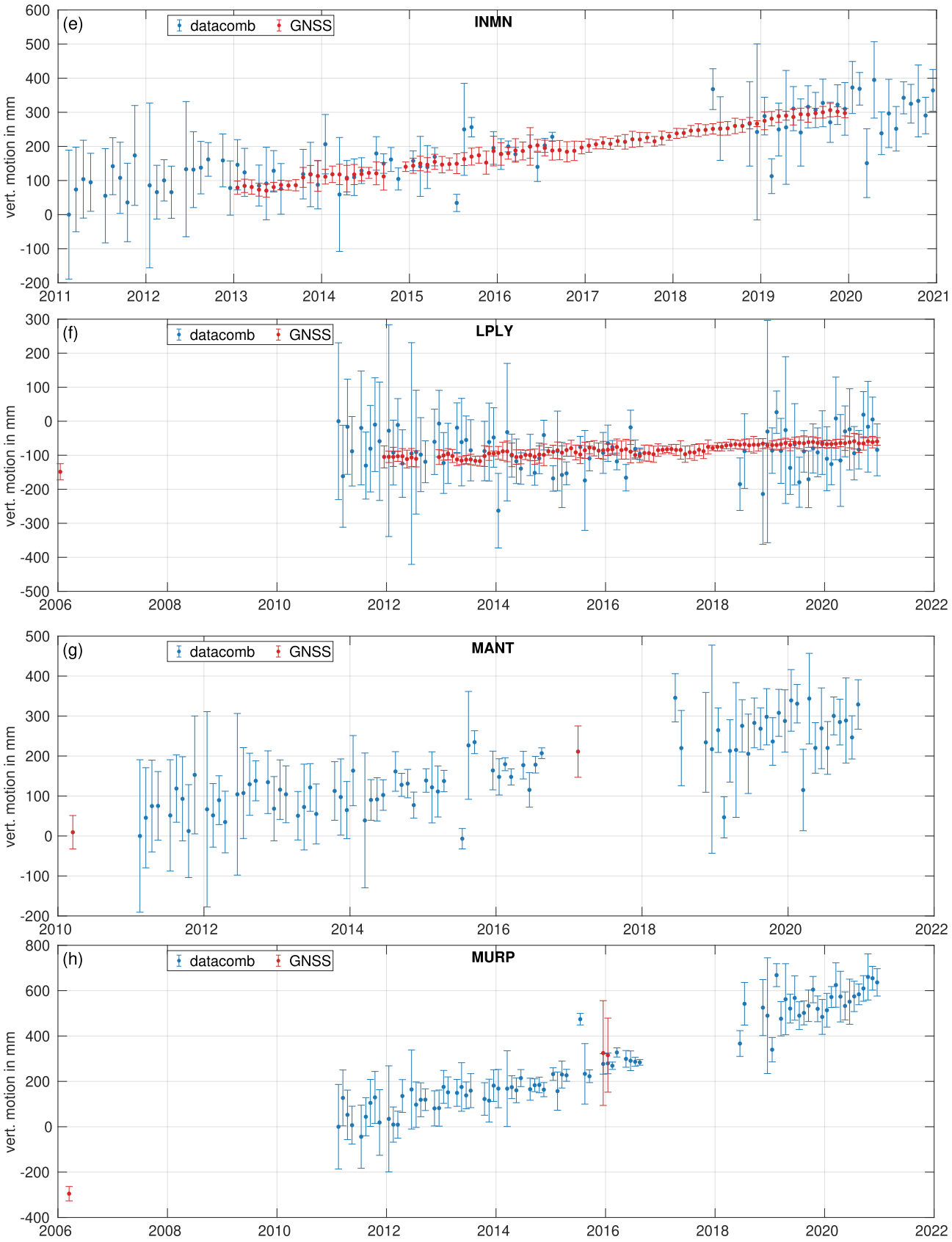
(e)
datacomb
GNSS
INMN
vert. motion in mm
(f)
LPLY
(g)
MANT
(h)
MURP

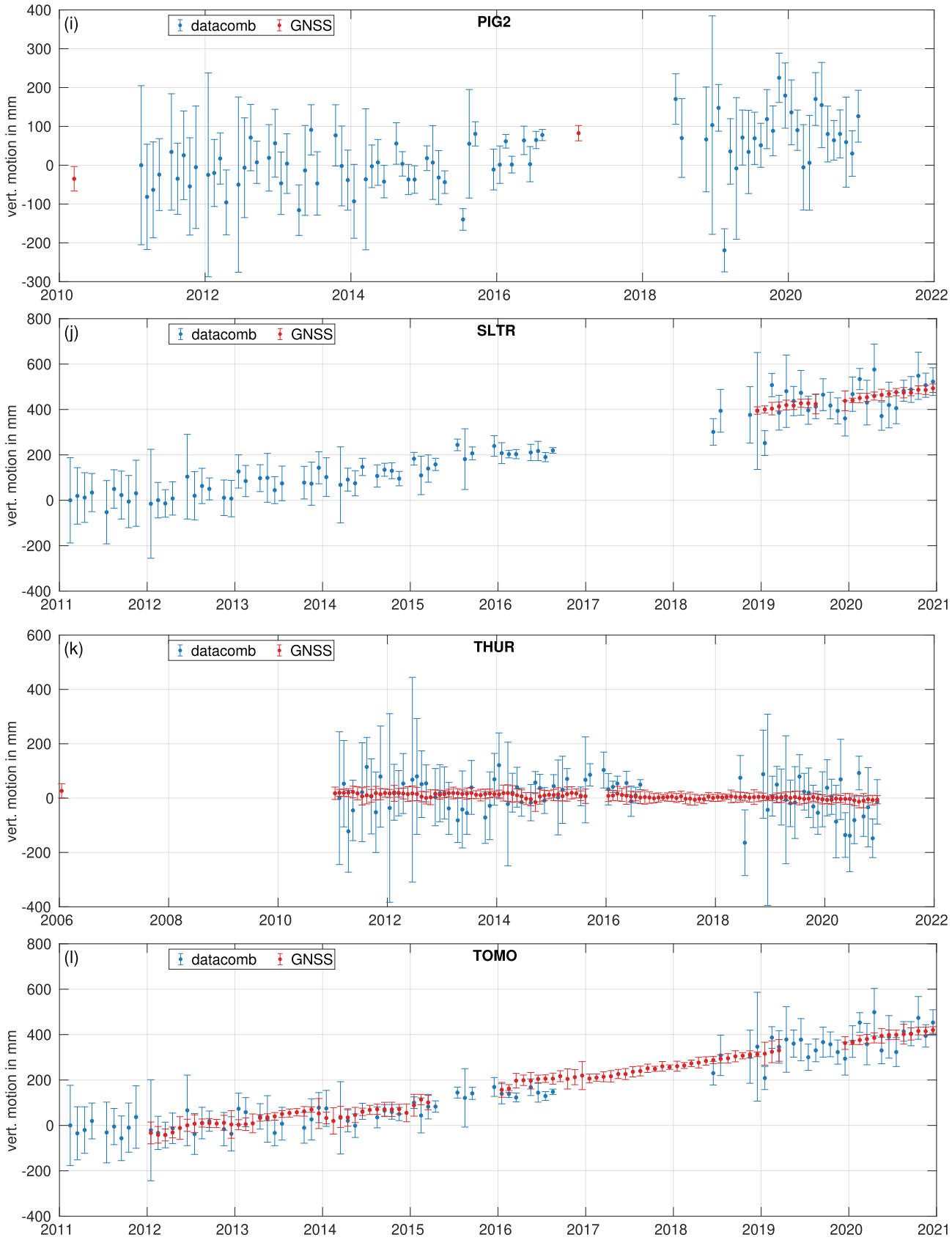
(i)
datacomb
GNSS
PIG2
vert. motion in mm
(j)
SLTR
(k)
THUR
(l)
TOMO

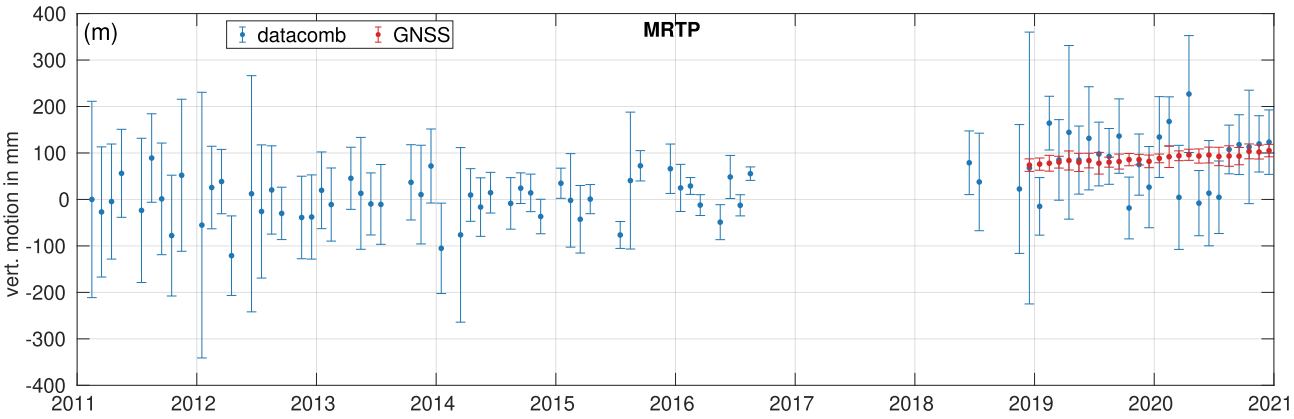

Figure S6: Comparison on time-series level of bedrock motion with 2-σ-uncertainties derived from the data combination (blue) and from GNSS measurements (red) at all GNSS sites (Table 1).

References

Barletta, V.R., M. Bevis, B.E. Smith, T. Wilson, A. Brown, A. Bordoni, M.Willis, S.A. Khan, M. Rovira-Navarro, I. Dalziel, R. Smalley, E. Kendrick, S. Konfal, D.J. Caccamise, R.C. Aster, A. Nyblade, and D.A. Wiens (2018). "Observed rapid bedrock uplift in Amundsen Sea Embayment promotes ice-sheet stability". In: *Science* 360.6395, pp. 1335–1339. DOI: 10.1126/science.aao1447.

Riva, R.E.M., B.C. Gunter, T.J. Urban, Bert L.A. Vermeersen, R.C. Lindenbergh, M.M. Helsen, J.L. Bamber, R.S.W. van de Wal, M.R. van den Broeke, and B.E. Schutz (2009). "Glacial Isostatic Adjustment over Antarctica from combined ICESat and GRACE satellite data". In: *Earth and Planetary Science Letters* 288.3-4, pp. 516–523. DOI: 10.1016/j.epsl.2009.10.013.

Sasgen, I., A. Martín-Español, A. Horvath, V. Klemann, E.J. Petrie, B. Wouters, M. Horwath, R. Pail, J.L. Bamber, P.J. Clarke, H. Konrad, and M.R. Drinkwater (2017). "Joint inversion estimate of regional glacial isostatic adjustment in Antarctica considering a lateral varying Earth structure (ESA STSE Project REGINA)". In: *Geophys. J. Int.* 211.3, pp. 1534–1553. ISSN: 0956-540X. DOI: 10.1093/gji/ggx368.

Willen, M.O., M. Horwath, A. Groh, V. Helm, B. Uebbing, and J. Kusche (2022). "Feasibility of a global inversion for spatially resolved glacial isostatic adjustment and ice sheet mass changes proven in simulation experiments". In: *J. Geod.* 96.10, pp. 1–21. ISSN: 0949-7714. DOI: 10.1007/s00190-022-01651-8.